



ELSEVIER

Nuclear Instruments and Methods in Physics Research A 480 (2002) 470–487

**NUCLEAR
INSTRUMENTS
& METHODS
IN PHYSICS
RESEARCH**
Section A

www.elsevier.com/locate/nima

A study on yttrium doping in lead tungstate crystals

Xiangdong Qu^a, Liyuan Zhang^a, Ren-Yuan Zhu^{a,*}, Jingying Liao^b,
Dingzhong Shen^b, Zhiwen Yin^b

^aCalifornia Institute of Technology, Pasadena, CA 91125, USA

^bShanghai Institute of Ceramics, Shanghai 200050, People's Republic of China

Received 23 February 2001; received in revised form 5 April 2001; accepted 7 April 2001

Abstract

In this paper we present results of a study on the yttrium doping in lead tungstate crystals. The crystal growth by modified Bridgman method is described. Results of trace analysis on raw materials and crystals are presented. The segregation coefficient of yttrium ions in lead tungstate crystals was determined. The scintillation emission and longitudinal transmittance spectra, light output, decay kinetics, light response uniformity and radiation damage were measured. It is found that yttrium doping suppresses slow scintillation component and improves radiation hardness of lead tungstate crystals. © 2002 Elsevier Science B.V. All rights reserved.

PACS: 81.10; 81.40

Keywords: Modified Bridgman method; Crystal growth; Lead tungstate; Doping; Radiation hardness

1. Introduction

Because of its high density and fast decay time, lead tungstate (PbWO₄) crystal was chosen by the Compact Muon Solenoid (CMS) experiment to construct a precision electromagnetic calorimeter (ECAL) at the Large Hadronic Collider (LHC) [1]. Good radiation hardness, however, is required for the use of PbWO₄ crystals in the CMS ECAL since the radiation level at LHC is expected to be up to 15 and 500 rad/h in barrel and endcaps respectively [2]. An effort has been made in the last five years at Shanghai Institute of Ceramics (SIC),

Shanghai, China, and Beijing Glass Research Institute (BGRI), Beijing, China, to develop radiation hard PbWO₄ crystals for applications in severe radiation environment, e.g. the CMS experiment. Our previous studies have led to an assumption that the radiation damage in PbWO₄ crystals is caused by host structure defects, such as oxygen or lead vacancies [3,4], which introduce local charge imbalance and trap electrons or holes and thus form color centers.

One approach to reduce the density of host structure defects is to optimize the stoichiometric ratio between two oxide raw materials and make a stringent control during crystal growth. This approach was taken by SIC and BGRI as well as other groups [5,6]. It is found that this optimization alone is not sufficient to reach required radiation hardness for CMS. Various approaches

*Corresponding author. Lauritsen Laboratory of High Energy Physics 256-48, Caltech, Pasadena, CA 91125, USA. Tel.: +1-626-395-6661; fax: +1-626-795-3951.

E-mail address: zhu@hep.caltech.edu (R.-Y. Zhu).

to suppress or compensate the remaining defects were tried. Oxygen compensation, referring to post-growth annealing at high temperature in an oxygen rich atmosphere, was found to be effective at SIC [7], indicating the main mechanism of radiation damage in PbWO_4 is oxygen vacancies, i.e. caused by electron centers.

Doping during crystal growth is another approach to either artificially introduce local charge imbalance and thus compensate structure defects or function as scavenger to further eliminate harmful impurities. In developing BGO crystals for the L3 experiment, europium doping was used at SIC to improve its radiation resistance [8]. In developing CsI(Tl) crystals for the *BaBar* and BELLE experiments, a special scavenger was used at SIC to remove oxygen contamination [7]. Pentavalent (Nb) doping in PbWO_4 was first reported by Lecoq et al. to be effective in improving transmittance at 100 ppm level [9]. Trivalent (La) doping was first reported by Kobayashi et al. to be effective in improving both transmittance [10] and radiation hardness [11]. Consequent studies found doping with various ions, such as La, Lu, Gd, Y and Nb, at optimized level to be effective in improving transmittance as well as radiation hardness [12,13].

Along the same direction, doping in PbWO_4 was extensively studied at SIC and BGRI. An early attempt of lanthanum (La) doping revealed that it indeed improved transmittance and reduced slow scintillation component, but La doped PbWO_4 crystals suffered from large dose dependence caused by shallow radiation induced color centers [14]. The very large (> 2) segregation coefficient of La in PbWO_4 crystals also makes it very difficult to produce a uniform La distribution in PbWO_4 crystals. Following that, doping with antimony (Sb) was tried at SIC. Since Sb ions exist in both trivalent and pentavalent forms it was hoped that both electron and hole centers might be compensated by using a single dopant. The result, however, showed that Sb doping alone was not sufficient to produce radiation hard PbWO_4 crystals, and post-growth oxygen compensation is required to make Sb doped PbWO_4 crystals radiation hard [15]. This indicates that Sb doping does not make effective compensation for the

intrinsic oxygen vacancies in PbWO_4 crystals. The very small segregation coefficient (0.052 ± 0.004) of Sb in PbWO_4 also makes it difficult to be implemented. Finally, yttrium (Y) doping was tried. The Y distribution in PbWO_4 crystals was found to be rather uniform with a segregation coefficient of 0.91 ± 0.04 . Y doped crystals were found to have fast scintillation light and adequate radiation hardness for CMS. This paper presents growth of Y doped crystals by modified Bridgman method and discusses their optical properties and radiation hardness.

2. Growth of Y doped PbWO_4 crystals

PbWO_4 crystals were grown by modified Bridgman method in SIC and BGRI. Raw materials of high purity, PbO and WO_3 , are produced in Shanghai, and are mixed in precise stoichiometric proportion of PbWO_4 in an agate mortar. The mixture is first melted in a platinum crucible in air to ensure complete homogeneity. After heated to high temperature this melt is sintered into a platinum crucible to form polycrystalline PbWO_4 grogs for crystal growth. Fig. 1 shows a schematic of a crucible used at SIC and BGRI for PbWO_4 crystal growth by modified Bridgman method.

At SIC and BGRI, multiple crucibles with individual computer controlled temperature profile are constructed in each furnace, allowing multi-pullings in one furnace. The layout of the furnace and its temperature profile can be found in Ref. [16]. Fig. 2 is a schematic showing a typical furnace with 28 crucibles for PbWO_4 growth. Furnaces of this kind were developed during 1980s at SIC for growth of BGO crystals for the L3 experiment at LEP, and were later successfully adapted for growth of CsI(Tl) crystals for the *BaBar* and BELLE experiments, and for growth of PbWO_4 crystals for the CMS experiment.

The stability of temperature field in furnace is crucial for successful growth of large size crystals. The temperature in these furnaces was monitored by Pt–Pt/Rh thermocouples and controlled by a DWT-702 temperature controller. During crystal growth the variation of temperature is required to be less than 0.5°C , which stabilizes the crystal

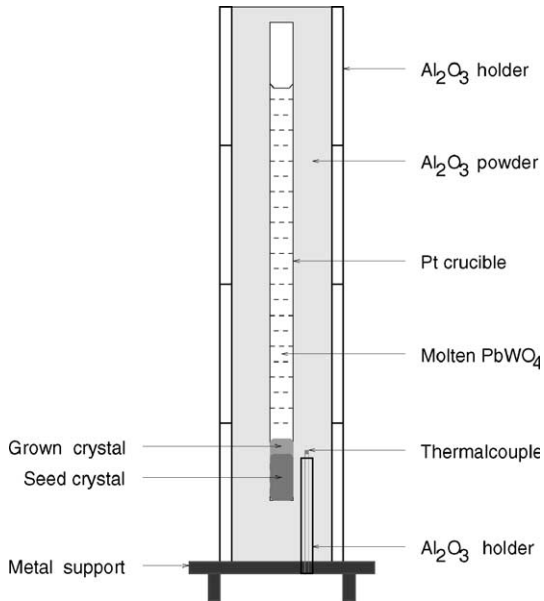


Fig. 1. A schematic showing a crucible used for PbWO_4 crystal growth by modified Bridgman method at SIC and BGRI.

growth rate and reduces the density gradient in the diffusion layer at the solid–liquid interface so that the density of constitutional super-cooling defects is minimized.

Crystals were grown along the c axis at SIC and BGRI. Twenty-eight crucibles of rectangular shape are constructed in every furnace for CMS PbWO_4 crystal growth. This shape of crucible makes efficient use of raw material since only a small fraction of ingot needs to be cut off to make final dimension. As-grown PbWO_4 crystals are transparent, colorless and without visible defects, such as cracking, inclusions, scattering centers and growth striation.

2.1. Raw materials

The identification of impurities, defects and structural changes is crucial for PbWO_4 crystal development since they are possibly responsible for the blue absorption, the slow decay components and the susceptibility to the radiation damage.

Raw materials used to grow scintillation crystals are required to have high purity, preferably 5N or 6N. The high cost, however, prevents the use of material of extra high purity. Research is needed to find and selectively remove harmful impurities. Various material characterization means are available to determine trace elements in raw material as well as crystals. Among them the Glow Discharge

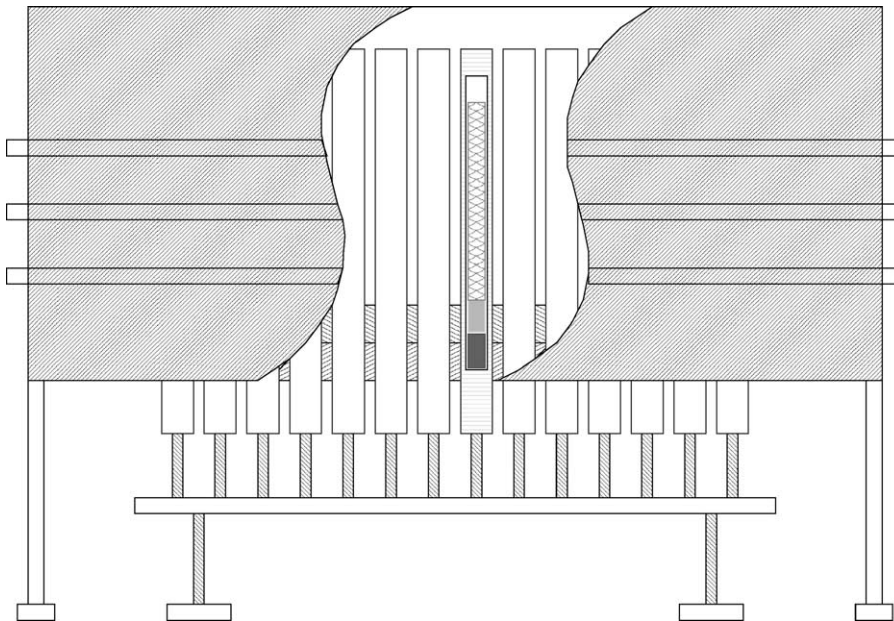


Fig. 2. A schematic of a typical Bridgman furnace with 28 crucibles.

Table 1
Results of GDMS analysis (ppmw) for raw materials

Raw material	PbO			WO ₃		
	04/1998	11/1998	03/1999	04/1998	11/1998	03/1999
Na	0.08	0.03	0.02	0.15	0.07	0.07
Mg	0.01	0.01	0.05	0.04	0.01	<0.01
Al	0.70	0.42	0.85	0.22	0.22	0.30
Si	0.15	0.12	0.27	0.15	0.25	0.25
K	0.15	0.06	<0.05	0.23	0.32	0.11
Ca	<0.05	0.18	0.22	0.36	0.11	<0.07
Mo	0.01	0.03	<0.01	0.61	0.61	0.20
Sb	<0.05	<0.05	<0.05	0.20	<0.05	<0.05
TM ^a	0.50	<0.30	<0.40	1.10	<1.00	<0.40
RE ^b	<0.30	<0.50	<0.50	<0.20	<0.50	<0.30

^aSum of transition metals.

^bSum of rare earths.

Mass Spectroscopy (GDMS) analysis is commonly used. It surveys 77 elements in a sample, taken 3–5 mm below the surface of the crystal to avoid contamination, with a sensitivity at sub-ppm level for the metallic contamination.

Previous GDMS analysis revealed that cation, especially Mo, contamination is responsible for the slow scintillation component in PbWO₄, as reported early by Kobayashi et al. [17] and Zhu et al. [3]. Since Mo is naturally contaminated in WO₃, special effort was made to reduce its contamination. After removing Mo and other cation contamination, PbWO₄ crystals produced at SIC and BGRI have significantly reduced slow component.

Table 1 lists GDMS analysis result, in part per million weight (ppmw), of trace impurities in raw materials of different batches produced since 1998. Also listed are the dates when these raw materials were produced and the sum of the transition metals (TM): Sc, Ti, V, Cr, Mn, Fe, Co, Ni, Cu and Zn, and the sum of the rare earth elements (RE): Ce, Pr, Nd, Eu, Sm, Gd, Tb, Dy, Ho, Er, Tm, Yb and Lu. The Mo contamination is found to be less than 1 ppm. This result of GDMS analysis shows that raw materials used at SIC have stable high purity.

2.2. Yttrium distribution in PbWO₄ crystals

Table 2 lists impurities (ppmw) found in several pairs of yttrium doped PbWO₄ samples

cut from the seed and tail ends of the same ingot. It shows that impurities Na, K, Cu, As and Mo migrated to the tail end of ingots during growth, indicating that their segregation coefficient in PbWO₄ crystals is less than one. The Ca, as well as La [14], is concentrated at the seed end with segregation coefficient of larger than one. The distribution of the yttrium, however, is rather uniform and is slightly less than 150 ppm mol of Y₂O₃ in melt, indicating that its segregation coefficient in PbWO₄ is less but close to 1.

Table 3 lists GDMS results of Y concentration (ppmw) in additional four pairs of samples taken at positions Z (cm) from the top (the tail end) of the ingot. Also listed is the initial Y concentration (ppmw) in the melt (Melt). The data in Tables 2 and 3 are used to extract the segregation coefficient of Y in PbWO₄.

The segregation coefficient k_e , defined as the ratio of the dopant concentration in the bulk crystal (C_{crystal}) to that in the melt (C_{melt}), describes the ability of the dopant to be incorporated into the solid phase:

$$k_e = \frac{C_{\text{crystal}}}{C_{\text{melt}}}. \quad (1)$$

Assuming a slow, steady state growth process, the distribution of a dopant concentration in a crystal

Table 2
Results of GDMS analysis (ppmw) for Y doped PbWO₄ ingots

Element	Seed/Tail 1	Seed/Tail 2	Seed/Tail 3	Seed/Tail 4	Tail 5
Na	0.2/0.8	0.2/1.0	0.4/0.8	0.2/1.8	0.8
Si	0.5/0.2	0.7/1.3	0.5/1.2	0.5/0.1	0.05
K	0.3/1.8	0.4/1.4	0.7/1.2	0.5/2.0	1.3
Ca	0.9/<0.05	0.6/0.08	0.12/0.15	0.6/0.2	0.15
Cu	0.04/0.2	0.04/0.4	0.3/0.35	0.08/0.54	0.23
As	0.15/0.35	0.1/0.6	0.5/0.5	0.2/0.6	0.54
Y	40/45	40/50	30/35	40/60	50
Mo	0.3/0.55	0.3/0.9	0.6/0.8	0.2/0.8	1.0
Nb	<0.05/<0.05	<0.05/<0.05	<0.05/<0.05	<0.05/<0.05	<0.05/<0.05
Sb	<0.05/<0.05	<0.05/<0.05	<0.05/<0.05	<0.05/<0.05	<0.05
La	<0.01/<0.01	<0.01/<0.01	<0.01/<0.01	<0.01/<0.01	<0.01

can be expressed as

$$C_{\text{crystal}}(g) = k_e \frac{C_0 - \int_0^g C_{\text{crystal}}(t) dt}{1 - g} \quad (2)$$

where C_0 is the initial dopant concentration in the melt, g is the relative solidification coefficient, defined as the ratio of the volume of solidification part of the ingot to the whole volume of the melt. The solution of Eq. (2) is

$$C_{\text{crystal}} = k_e C_0 (1 - g)^{k_e - 1}. \quad (3)$$

Taking logarithm, Eq. (3) can be written as a linear equation:

$$\ln \frac{C_{\text{crystal}}}{C_0} = \ln k_e + (k_e - 1) \ln(1 - g). \quad (4)$$

Fig. 3 shows a linear fit to the GDMS data. The numerical result of the effective segregation coefficient of yttrium ions in PbWO₄ crystals was found to be 0.91 ± 0.04 . This rather uniform distribution of the yttrium concentration in PbWO₄ crystals makes it a good dopant.

3. Properties of Y doped PbWO₄ crystals

Optical properties of 16 yttrium doped PbWO₄ crystals were characterized at Caltech. All samples are CMS full size with a tapered shape: 2.6 cm × 2.6 cm at the large end, tapering to 2.2 cm × 2.2 cm at the small end, and 23 cm long. Table 4 lists dimension, the dopant, the peak wavelengths of the photoluminescence (λ_{pho}) and radiolumine-

Table 3
GDMS results of Y concentration (ppmw) in PbWO₄ samples

ID	699	699	723	723	727	727	743	743
Melt	29.3	29.3	29.3	29.3	29.3	29.3	29.3	29.3
Z	5.5	29.0	3.0	26.5	4.0	28.0	4.5	28.0
Y	39	29	38	30	30	24	31	20

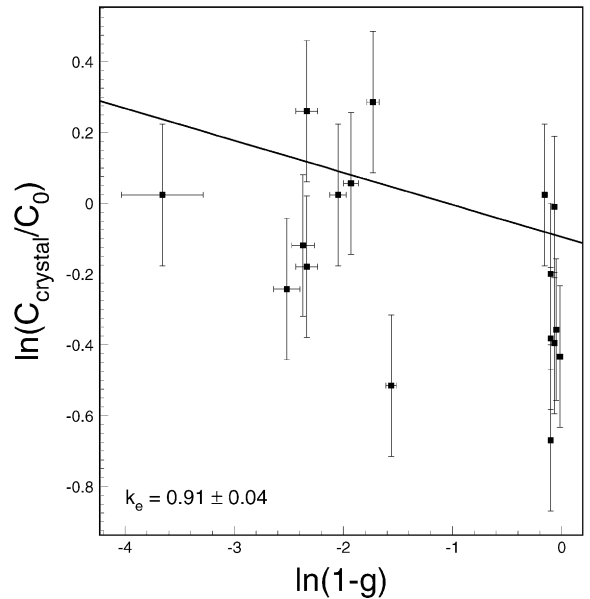


Fig. 3. A linear fit to the logarithm of yttrium concentration in PbWO₄ crystals.

science (λ_{rad}) and the date on which the sample was received. Samples denoted with SIC and BGRI were grown at SIC and BGRI respectively by

Table 4
Y doped PbWO₄ crystal samples

ID	Dimension (cm)	Dopant	λ_{pho} (nm)	λ_{rad} (nm)	Date
SIC-S301	2.2 × 23.0 × 2.6	Y/Sb	420	445	06/08/1999
SIC-S347	2.2 × 23.0 × 2.6	Y/Sb	420	445	06/08/1999
SIC-S392	2.2 × 23.0 × 2.6	Y	420	445	06/08/1999
SIC-S412	2.2 × 23.0 × 2.6	Y	420	445	06/08/1999
SIC-S643	2.2 × 23.0 × 2.6	Y	420	445	11/30/1999
SIC-S762	2.2 × 23.0 × 2.6	Y	420	445	08/25/2000
SIC-606	2.2 × 23.0 × 2.6	Y	420	445	11/30/1999
SIC-678	2.2 × 23.0 × 2.6	Y	420	445	08/25/2000
SIC-679	2.2 × 23.0 × 2.6	Y	420	445	08/25/2000
BGRI-824	2.2 × 23.0 × 2.6	Y	420	—	07/10/2000
BGRI-826	2.2 × 23.0 × 2.6	Y	420	—	07/10/2000
BTCP-2133	2.2 × 22.9 × 2.5	Y/Nb	420	435	04/01/1999
BTCP-2162	2.2 × 22.8 × 2.5	Y/Nb	420	435	04/01/1999
BTCP-5615	2.2 × 23.0 × 2.6	Y/Nb	420	435	08/25/2000
BTCP-5618	2.2 × 23.0 × 2.6	Y/Nb	420	435	08/25/2000
BTCP-5658	2.2 × 23.0 × 2.6	Y/Nb	420	435	08/25/2000

modified Bridgman method. Samples denoted with BTCP were grown at Bogoroditsk Techno-Chemical Plant, Russia, by the Czochralski method. While the chinese crystals were produced during the R&D phase, the russian crystals were grown during the preproduction phase. More detailed discussions on the equipment and techniques used for the optical property and light output measurement can be found in Ref. [3].

3.1. Photoluminescence and radioluminescence

Photoluminescence was measured by using a Hitachi F-4500 fluorescence spectrophotometer. A schematic of the measurement setup is shown in Fig. 4, where UV excitation light was shot to a bare surface of the sample and photoluminescence, without passing through the sample, was measured by a photomultiplier tube (PMT) through a monochromator. The setup used to measure radioluminescence is shown in Fig. 5, where whole body of a wrapped sample was irradiated by ⁶⁰Co γ -ray at a dose rate of about 1000 rad/h, and the radioluminescence, passing through the sample, was focused, passed through a monochromator and measured by a PMT.

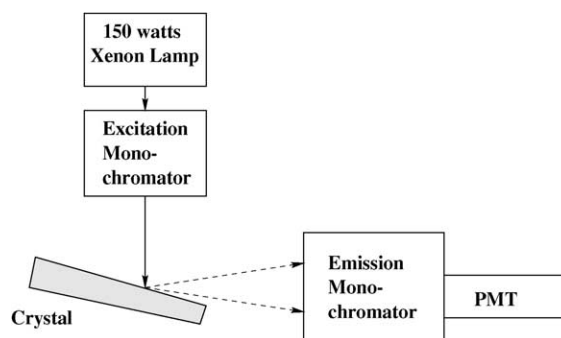


Fig. 4. A schematic of the setup used to measure photoluminescence.

The peak wavelengths of photoluminescence (λ_{pho}) and radioluminescence (λ_{rad}) are listed in Table 4. A comparison of photoluminescence (solid) and radioluminescence (dashed) spectra for four PbWO₄ samples is shown in Fig. 6. These spectra were corrected for the wavelength dependence of light source intensity, the monochromator grating efficiency and the photodetector quantum efficiency. The vertical axis refers to photon numbers, and its scale is arbitrary.

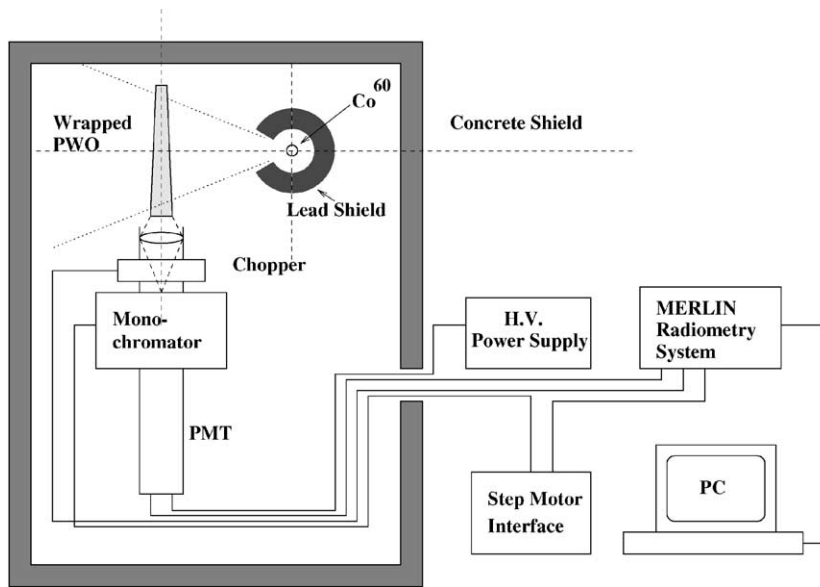


Fig. 5. A schematic of the setup used to measure radioluminescence.

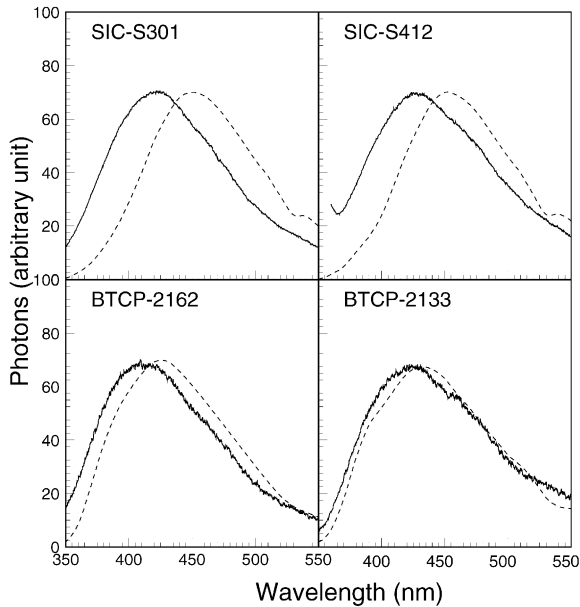


Fig. 6. A comparison of photoluminescence (solid lines) and radioluminescence (dashed lines) spectra for samples SIC-S301, SIC-S412, BTCP-2133 and BTCP-2162.

As seen from the figure the peak of the radioluminescence is 15–25 nm red shifted as compared to that of the photoluminescence. This

red shift is explained by the internal absorption since PbWO_4 transmittance at shorter wavelengths is poorer than that at longer wavelengths. A crosscheck of photoluminescence with a modified setup, where luminescence light passed through the sample, showed similar red shift, and thus confirmed this explanation. Since the photoluminescence spectrum measured with the setup in Fig. 4 is not affected by the internal absorption, it can be seen as the intrinsic emission spectrum, while the radioluminescence spectrum is a convolution of the intrinsic emission and the internal absorption with the latter depends on the light path. Measurement on the other sample shows that all Y doped PbWO_4 samples have a broad emission spectrum with a peak at about 420 nm.

It is interesting to note that both the excitation and emission spectra of PbWO_4 crystals are not affected by the γ -ray irradiation. Figs. 7 and 8 show the excitation and photoluminescence spectra before and after irradiations at 9 krad/h for samples SIC-S762 and BTCP-2133 respectively. Within the measurement errors the shapes of these spectra are identical. This observation is consistent with our previous conclusion that the scintillation mechanism in PbWO_4 crystals is not damaged by the irradiation [3,18].

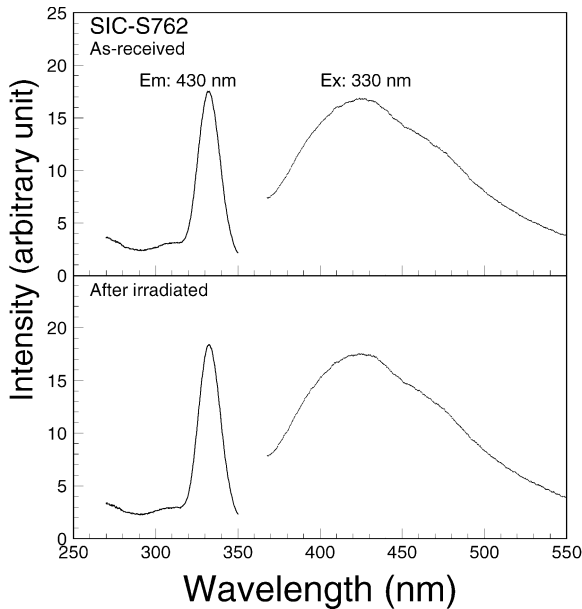


Fig. 7. Excitation and photoluminescence spectra are shown before and after γ -ray irradiations at 9 krad/h for sample SIC-S762.

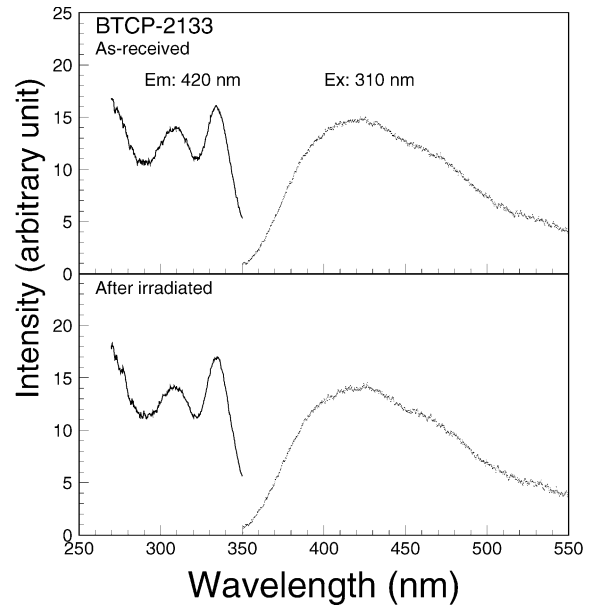


Fig. 8. Excitation and photoluminescence spectra are shown before and after γ -ray irradiations at 9 krad/h for sample BTCP-2133.

3.2. Light output and decay kinetics

The scintillation light output and decay kinetics were measured using a Hamamatsu PMT R2059, which has a bi-alkali photocathode and a quartz window. For measurements of the light output the large end of a sample was coupled to the PMT with Dow Corning 200 fluid, while all the other faces of the sample were wrapped with Tyvek paper. A collimated ^{137}Cs source was used to excite the sample. The γ -ray peak was obtained by a simple Gaussian fit, and was used to determine photoelectron numbers by using calibrations of the single photoelectron peak.

All measurements were carried out at room temperature of 20°C . Data were corrected by using the room temperature which has daily variations of up to 0.5°C , despite central air condition of entire building and individual temperature adjustment and feedback in the laboratory where measurement was carried out. This variation is significant since the light output of PbWO_4 crystals is known to have $-2\%/^\circ\text{C}$ at the room temperature. The systematic uncertainty of the

light output measurement, including the temperature variation and the operation uncertainties caused by mounting samples to the PMT, was estimated to be about 1%. Fig. 9(a) shows the repeated measurement of the light output for a sample in 9 h. Fig. 9(b) and (c) shows raw and temperature corrected light output and corresponding Gaussian fit, respectively. Precisions of 1% and 0.8% were achieved for the light output measurement without and with temperature corrections respectively.

Figs. 10 and 11 show light output as a function of integrated time. Data in these figures are in units of number of photoelectrons per MeV of energy deposition (p.e./MeV). The ratio between light outputs integrated to 100 and 1000 ns is about 95%, as compared to 90% and 85% for Sb doped and undoped PbWO_4 crystals respectively [15].

3.3. Longitudinal transmittance

Longitudinal transmittance was measured by using a Hitachi U-3210 UV/visible

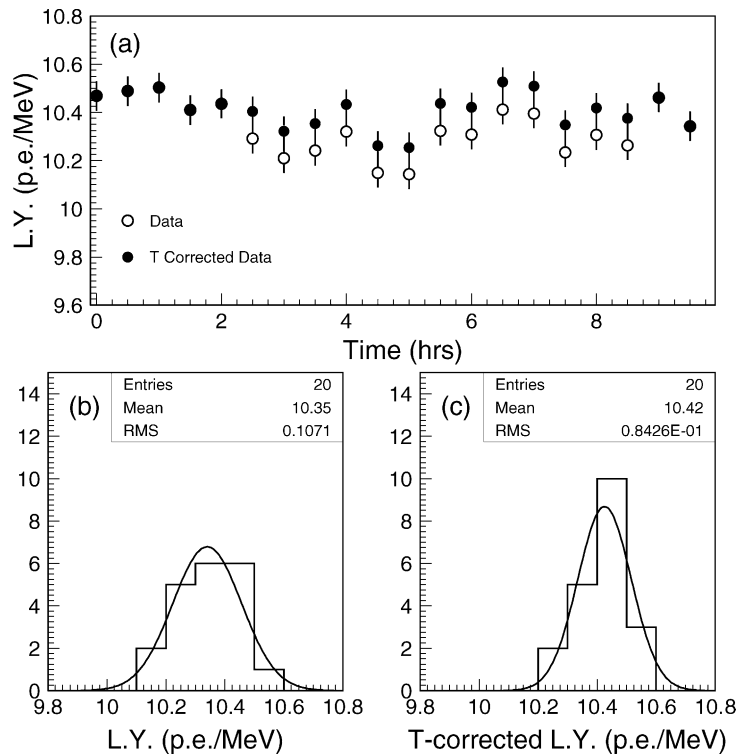


Fig. 9. (a) Light output measured by the PMT through a LeCroy QVT, taken in 9 h, and its distributions (b) without and (c) with temperature corrections.

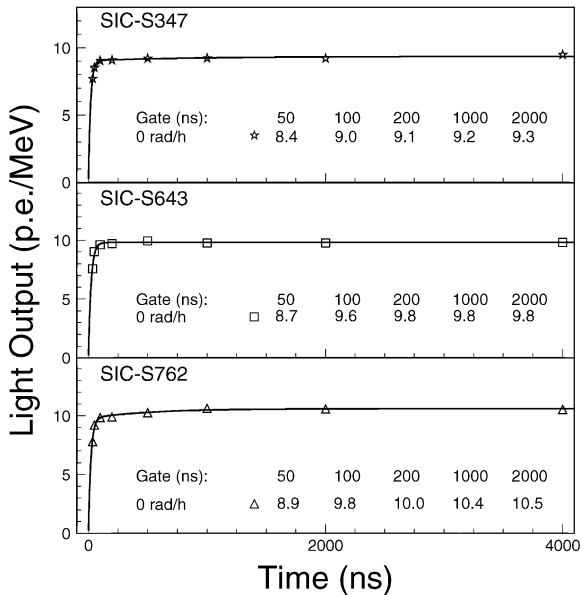


Fig. 10. Light output of three SIC samples is shown as a function of integration time.

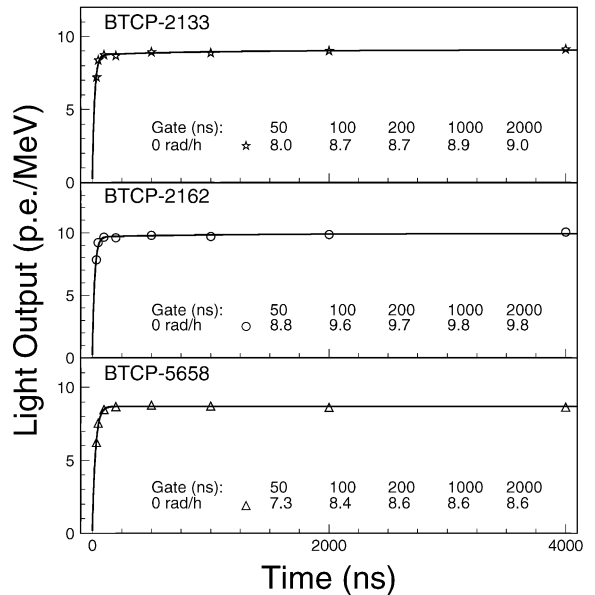


Fig. 11. Light output of three BTCP samples is shown as a function of integration time.

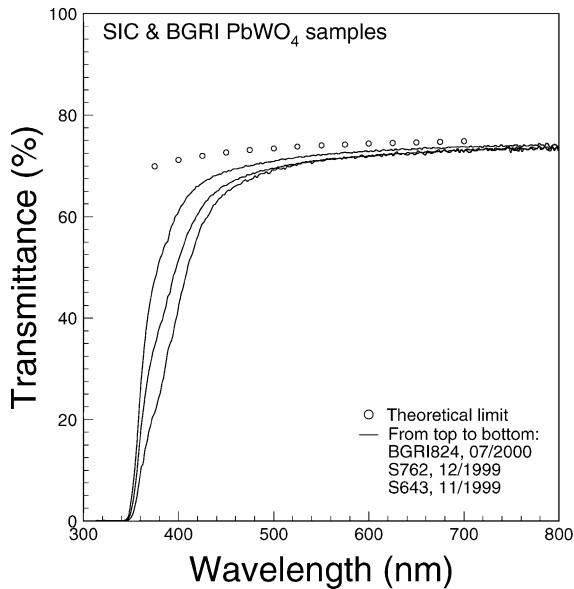


Fig. 12. Longitudinal transmittance is shown as a function of wavelength for three chinese samples, compared to the theoretical limit (circles).

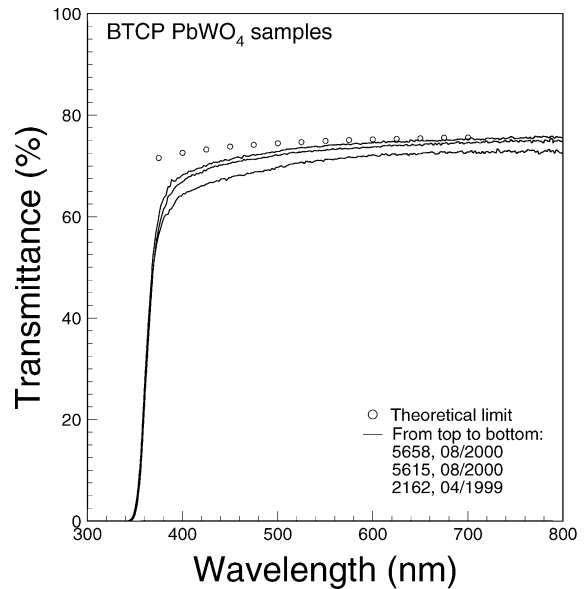


Fig. 13. Longitudinal transmittance is shown as a function of wavelength for three russian samples, compared to the theoretical limit (circles).

spectrophotometer with double beam, double monochromator and a large sample compartment equipped with a custom Halon coated integrating sphere. The systematic uncertainty in repeated measurements is about 0.3%.

Figs. 12 and 13 show the longitudinal transmittance as a function of wavelength for three PbWO_4 samples each from China and Russia respectively. Also shown in these figures is the theoretical limit of the transmittance calculated by using the refractive index of the ordinary and extraordinary polarization light [3,19]. At the emission peak, 420 nm, the transmittance of the extraordinary light is about 3% higher than that of the ordinary light. Chinese crystals are grown along the c axis, so its theoretical limit of transmittance was calculated by using refractive index of the ordinary polarization light. Russian crystals are grown along the a axis, so its theoretical limit of transmittance was calculated by using a combination of the refractive indexes of the ordinary and extraordinary polarization components. Both russian and chinese crystals approach theoretical limit, indicating very low residual absorption.

Improvements of longitudinal transmittance during the R&D phase for chinese crystals and during the preproduction phase for russian crystals are observed. It is also noticed that early samples grown in China have a low transmittance at short wavelength caused by scattering centers, but no direct correlations between transmittance and the radiation hardness were observed. A fine tuning of growth parameters improved transmittance at short wavelength, as shown in Fig. 12.

4. Radiation damage

The optical properties and light output of these samples were characterized at Caltech both before and after irradiations. All irradiations were carried out by using a ^{60}Co γ -ray source of 50 C. During irradiation, samples were wrapped with Tyvek paper and aluminum foil, and were placed at a fixed distance to the source, so that the entire body of the sample is under defined dose rate. Samples were under irradiation all the time, except when measurements were carried out, which typically

lasted for less than 1 h. All measurements on the samples after irradiation were carried out in the dark to minimize optical bleaching effect.

4.1. Light output degradation and recovery

The degradation of crystal’s light output under irradiation is a direct measure of its radiation hardness. To reduce systematic uncertainty the light output was defined as an average of several measurements with a collimated ¹³⁷Cs source shooting at evenly distributed positions along the sample. Nine measurements were used for samples of CMS size (23 cm), while five measurements were used for samples of 10 cm long.

It is known that radiation induced color centers are created in PbWO₄ crystals by irradiation, and may annihilate in room temperature. During irradiation, both annihilation and creation processes coexist, the color center density reaches an equilibrium at a level depending on the dose rate applied. Assuming the annihilation speed of the color center *i* is proportional to a constant *a_i* and its creation speed is proportional to a constant *b_i* and the dose rate (*R*), the differential variation of color center density when both processes coexist can be written as [7]

$$dD = \sum_{i=1}^n \{-a_i D_i + (D_i^{all} - D_i) b_i R\} dt \quad (5)$$

where *D_i* is the density of the color center *i* in the crystal and the summation goes through all centers. The solution of Eq. (5) is

$$D = \sum_{i=1}^n \left\{ \frac{b_i R D_i^{all}}{a_i + b_i R} [1 - e^{-(a_i + b_i R)t}] + D_i^0 e^{-(a_i + b_i R)t} \right\} \quad (6)$$

where *D_i^{all}* is the total density of the trap related to the center *i* and *D_i⁰* is its initial density. The color center density in equilibrium (*D_{eq}*) depends on the dose rate (*R*) applied:

$$D_{eq} = \sum_{i=1}^n \frac{b_i R D_i^{all}}{a_i + b_i R} \quad (7)$$

Figs. 14 and 15 show light output normalized to that before irradiation (solid dots with error bars) as a function of time under irradiation for samples

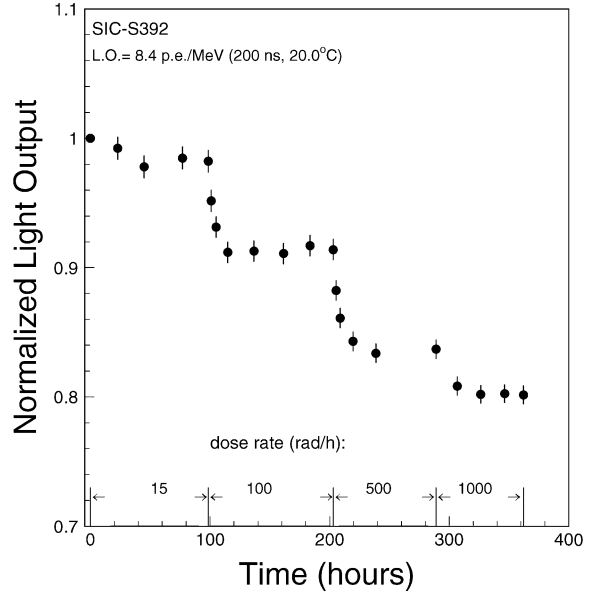


Fig. 14. Normalized light output is shown as a function of time under irradiations for sample SIC-S392.

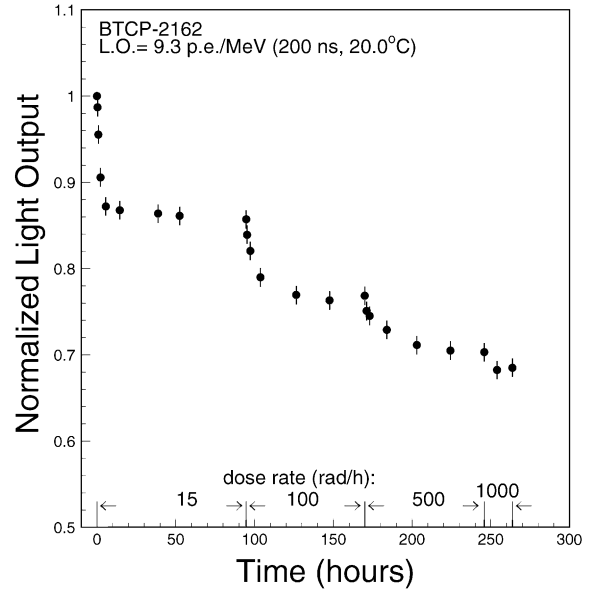


Fig. 15. Normalized light output is shown as a function of time under irradiations for sample BTCP-2162.

SIC-S392 and BTCP-2162. Measurements were done step by step for different dose rates: 15, 100, 500 and 1000 rad/h, as shown in these figures. The

Table 5
Summary of light output measurements

Sample ID	LO (1/MeV)		Fraction (%)		LO (%) at R (rad/h)			
	p.e.	γ	$\frac{50 \text{ ns}}{1 \mu\text{s}}$	$\frac{100 \text{ ns}}{1 \mu\text{s}}$	15	100	500	1000
SIC-S301	9.4	63.5	92.0	96.6	96.6	87.3	79.5	74.3
SIC-S347	9.9	66.9	91.3	97.8	95.1	88.6	82.1	78.0
SIC-S392	8.4	56.8	92.0	97.3	98.2	91.3	83.6	80.2
SIC-S412	8.3	56.1	94.6	98.6	98.2	91.2	85.9	85.3
SIC-S643	8.9	60.1	88.8	98.9	88.3	79.8	—	—
SIC-S762	10.6	71.6	85.6	94.2	91.5	84.2	81.4	—
SIC-606	10.4	70.3	88.3	98.4	91.7	79.3	—	—
SIC-678	10.4	70.3	85.2	93.5	94.2	76.0	59.6	—
SIC-679	10.8	73.0	85.0	94.7	93.5	73.5	57.3	—
BGRI-824	11.4	77.0	83.5	95.5	89.0	78.7	69.9	—
BGRI-826	11.2	75.7	84.4	96.7	86.0	74.7	62.2	—
BTCP-2133	8.2	55.4	89.9	97.8	89.2	78.6	72.3	70.5
BTCP-2162	9.3	62.8	89.8	97.9	86.1	76.8	70.3	68.2
BTCP-5615	7.2	48.6	86.6	98.5	82.9	—	—	—
BTCP-5618	7.2	48.6	86.8	98.5	77.4	—	—	—
BTCP-5658	8.8	59.5	83.9	97.7	76.1	63.6	—	—

degradation of the light output shows a clear dose rate dependence, as described by Eq. (7).

Table 5 summarizes the numerical results of the light output before irradiation and the normalized light output (%) in equilibrium under certain dose rates. The light output (LO), in units of number of photoelectrons per MeV energy deposit (p.e./MeV), is defined as the average of nine measurements with an integration time of 200 ns at 20.0°C. By using emission weighted quantum efficiencies of the R2059 PMT (14.8%), the measured light output was converted to the light yield in units of photons/MeV. It is clear that the loss of light output at the maximum dose rate at barrel (15 rad/h) is about 5–15%, which can be converted to 2–6% if irradiations were applied at the front (small) end of the crystal.

The radiation damage in PbWO₄ crystal recovers at room temperature. Since the light output of PbWO₄ crystals varies during both damage and recovery, a precision calibration is the key for maintaining the precision of crystal calorimetry in situ. For CMS PbWO₄ calorimeter the calibration is achieved by using physics processes combined

with the intercalibrations provided by a light monitoring system [2], which measures the variation of the transmittance to 0.1% at the peak wavelength of PbWO₄ emission [20,21]. The goal of the monitoring system is to provide an intercalibration to a precision of 0.4%. Since a complete monitoring run for entire calorimeter takes about 37 min [22], the variation speed for the light output, either during damage or during recovery, is preferred to be less than 1%/h.

Figs. 16 and 17 show the damage (dots with error bars, left scale), corresponding exponential fit (solid lines) and damage speed (dashed lines, right scale) of normalized light output under irradiation at 15 rad/h for samples SIC-S392 and BTCP-2162 respectively. Figs. 18 and 19 show the recovery (dots with error bars, left scale), corresponding exponential fit (solid line) and recovery speed (dashed lines, right scale) of normalized light output after an irradiation at 400 rad/h for samples SIC-S392 and BTCP-2162 respectively.

While the damage data were fit to

$$LY/LY_0 = 1 - b(1 - e^{-t/\tau}) \quad (8)$$

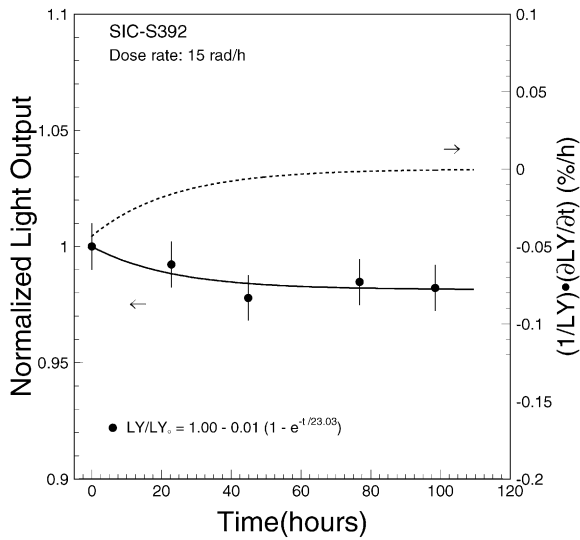


Fig. 16. Light output damage (dots with error bars, left scale) and damage speed (dashed lines, right scale) for sample SIC-S392.

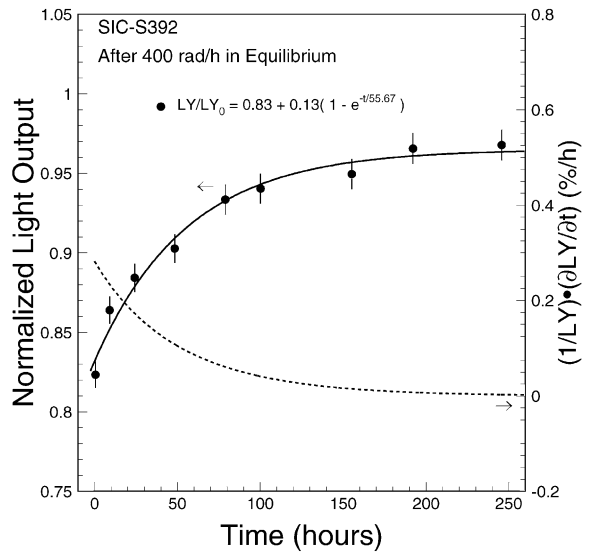


Fig. 18. Light output recovery (dots with error bars, left scale) and recovery speed (dashed lines, right scale) for sample SIC-S392.

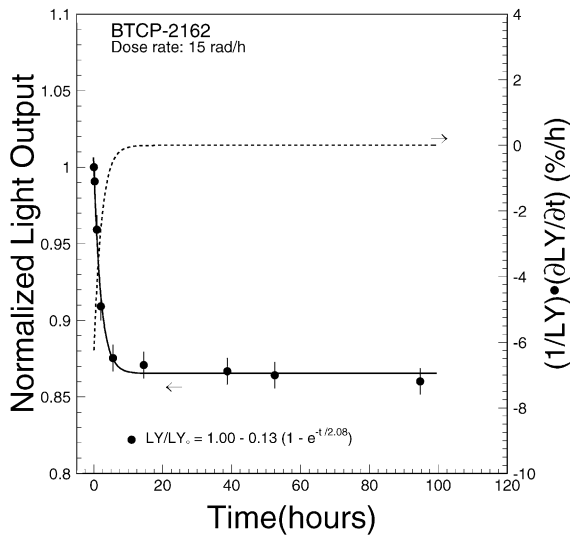


Fig. 17. Light output damage (dots with error bars, left scale) and damage speed (dashed lines, right scale) for sample BTCP-2162.

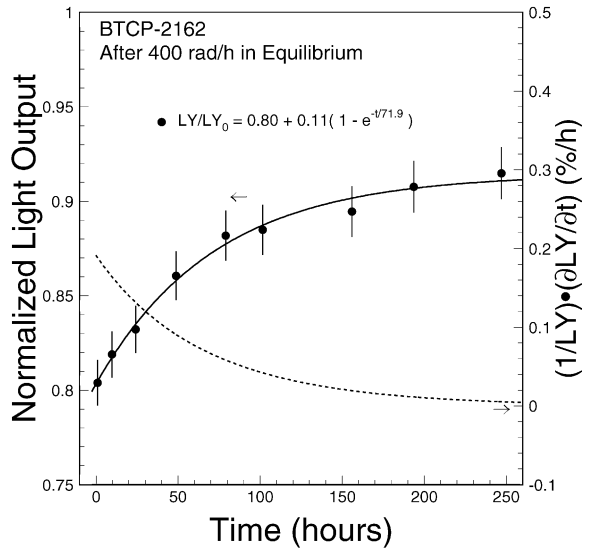


Fig. 19. Light output recovery (dots with error bars, left scale) and recovery speed (dashed lines, right scale) for sample BTCP-2162.

the recovery data were fit to

$$\begin{aligned}
 LY/LY_0 &= 1 - a - be^{-t/\tau} \\
 &= (1 - a - b) + b(1 - e^{-t/\tau})
 \end{aligned}
 \tag{9}$$

where a and b are two constants representing the amplitude of the slow and fast components respectively, and τ is the time constant of the fast component.

Table 6
Summary of PbWO₄ damage and recovery speed (%/h)

Sample ID	Damage under (rad/h)				Recovery from 400 rad/h
	15	100	400	1000	
SIC-S301	-0.21	-2.3	-4.9	-0.35	0.37
SIC-S347	-0.67	-0.54	-3.9	-0.28	0.27
SIC-S392	-0.04	-1.3	-1.6	-0.23	0.31
SIC-S412	-0.10	-0.82	-1.7	-0.81	0.19
SIC-S643	-1.0	-0.85	-1.4	—	0.41
SIC-S762	-3.0	-1.9	-3.6	—	0.04
SIC-606	-0.31	-0.53	-3.1	—	0.48
SIC-678	-1.1	-5.3	-9.0	—	0.59
SIC-679	-0.21	-4.8	-5.8	—	0.41
BGRI-824	-6.8	-2.3	-3.2	—	0.38
BGRI-826	-6.5	-4.6	-5.1	—	0.46
BTCP-2133	-5.5	-2.8	-0.75	-1.1	—
BTCP-2162	-6.3	-1.6	-0.51	-0.95	0.19
BTCP-5615	-10.8	—	—	—	—
BTCP-5618	-22.0	—	—	—	—
BTCP-5658	-16.4	-0.85	—	—	—

Table 6 lists the maximum speed (in units of %/h) of light output variation for the damage process under different dose rates and for the recovery process after reaching equilibrium at 400 rad/h. As shown in the table, some samples may have too fast damage speed under irradiation, indicating possible less accurate calibrations for a short time at the beginning.

4.2. Light response uniformity

While variations of the amplitude of the light output can be intercalibrated, the loss of the energy resolution, caused by the degradation of light response uniformity is not recoverable [18]. To preserve crystal's intrinsic energy resolution, the light response uniformity must be kept within tolerance. The light response uniformity was measured by moving a collimated γ -ray source along the longitudinal axis of a sample at nine points evenly distributed along the crystal and the response (y) was fit to a linear function

$$\frac{y}{y_{\text{mid}}} = 1 + \delta(x/x_{\text{mid}} - 1), \quad (10)$$

where y_{mid} represents the light response at the middle of the crystal, δ represents the deviation of the light response uniformity and x is the distance from the small (front) end of a tapered crystal.

Figs. 20 and 21 show the light response uniformity as a function of accumulated dose for samples SIC-S412 and BTCP-2133, respectively, where δ is a measure of the light response uniformity, as defined in Eq. (10). These figures show clearly that the slope (δ) and the shape of the uniformity do not change. This good uniformity can be attributed to the fact that the light attenuation length at the emission peak (420 nm) is long enough even after irradiation, which provides an adequate compensation between the attenuation and the focusing effect caused by crystal's tapered shape [18].

4.3. Longitudinal transmittance

Figs. 22 and 23 show the longitudinal transmittance as a function of wavelength measured before and after a series of irradiations for samples BGRI-824 and BTCP-5658, respectively. The curves in each plot in an order from the top to

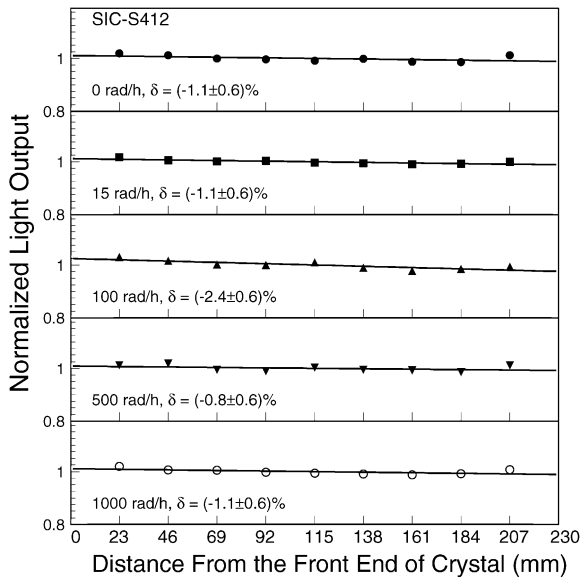


Fig. 20. The light response uniformities are shown as a function of integrated dose for sample SIC-S412.

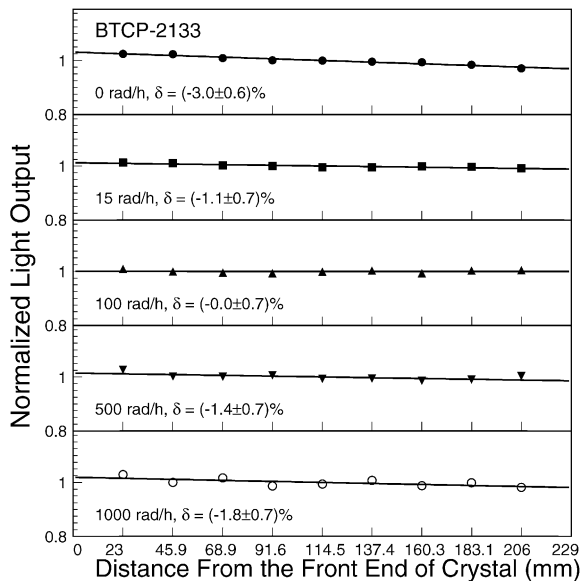


Fig. 21. The light response uniformities are shown as a function of integrated dose for sample BTCP-2133.

the bottom represent the transmittance before irradiation and that immediately after irradiation when they reached an equilibrium under specified

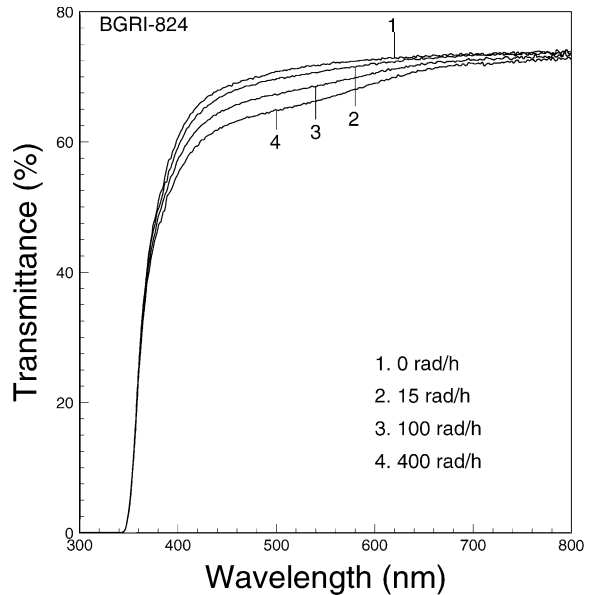


Fig. 22. Longitudinal transmittance is shown as a function of wavelength for sample BGRI-824 before and after irradiation.

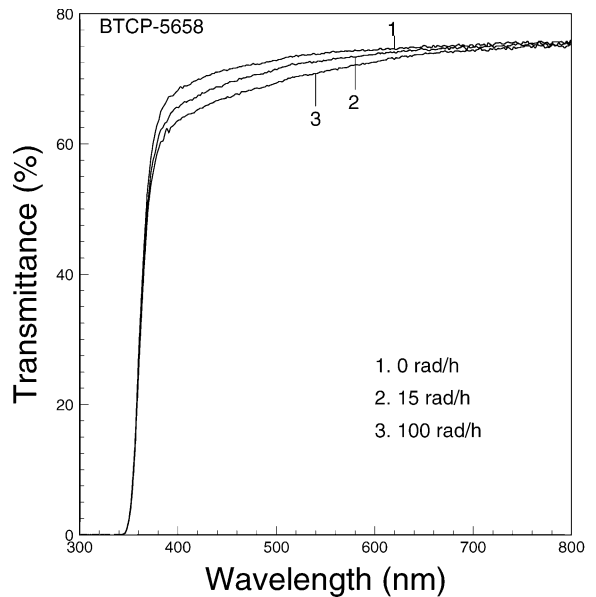


Fig. 23. Longitudinal transmittance is shown as a function of wavelength for sample BTCP-5658 before and after irradiation.

dose rate. It is interesting to note that these two samples have very similar behavior under irradiation. As discussed before [20] and in Section 4.4,

the radiation induced absorption in all Y doped samples can be decomposed into two common radiation induced color centers.

4.4. Radiation induced color centers

The longitudinal transmittance data can be used to calculate radiation induced color center density. Figs. 24 and 25 show radiation induced color center density as a function of photon energy measured for samples SIC-S392 and BTCP-2133, respectively in equilibrium at different dose rates. The stars in these figures represent corresponding radioluminescence spectra weighted with quantum efficiency of the PMT. The points with error bars in these figures are radiation induced color center density (D), or absorption coefficient, measured in equilibrium under dose rates specified. They were calculated according to an equation

$$D = 1/LAL_{\text{equilibrium}} - 1/LAL_{\text{before}}. \tag{11}$$

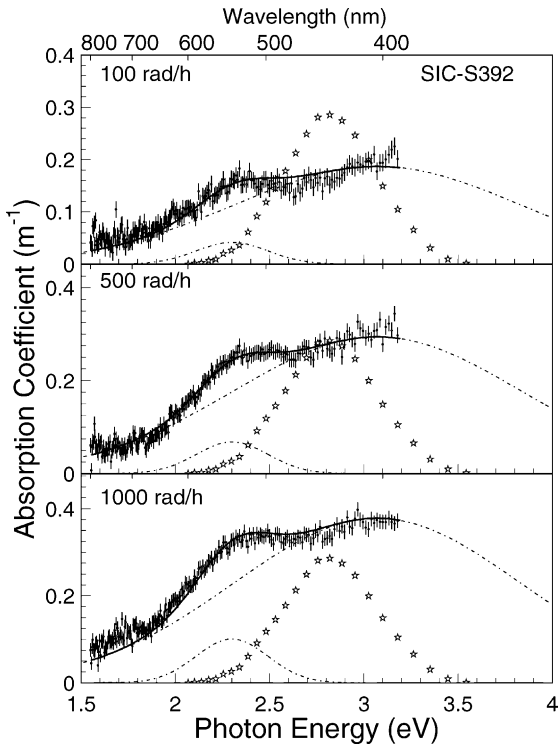


Fig. 24. Radiation induced color center density for sample SIC-S392.

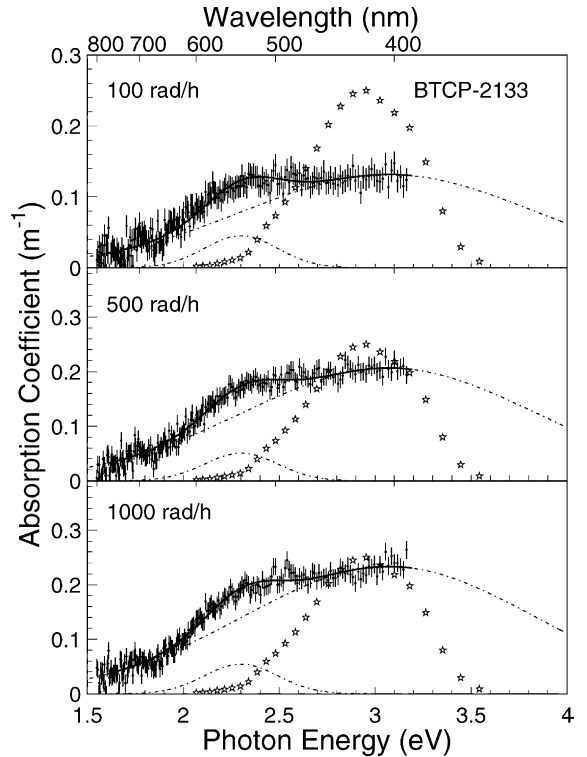


Fig. 25. Radiation induced color center density for sample BTCP-2133.

where LAL is the light attenuation length calculated by using longitudinal transmittance according to Eq. (1) of Ref. [3], and the subscripts “equilibrium” and “before” refer to “in equilibrium” and “before irradiation”, respectively. The radiation induced color center density was decomposed to a sum (solid line) of two color centers with Gaussian shape in photon energy (dashed lines):

$$D = \sum_{i=1}^2 A_i e^{-(E-E_i)^2/2\sigma_i^2} \tag{12}$$

where E_i , σ_i and A_i denote the energy, width and amplitude of the color center i , and E is the photon energy. As seen from these figures, the two center Gaussian fit provides a rather good description of the radiation induced color center data with good χ^2/DoF .

Table 7
Summary of radiation induced color centers

ID	E_1/σ_1 (eV/eV)	A_1^a (m^{-1})	A_1^b (m^{-1})	A_1^c (m^{-1})	A_1^d (m^{-1})	E_2/σ_2 (eV/eV)	A_2^a (m^{-1})	A_2^b (m^{-1})	A_2^c (m^{-1})	A_2^d (m^{-1})
SIC-S301	2.30/0.19	0.00	0.04	0.07	0.11	3.07/0.76	0.10	0.22	0.35	0.42
SIC-S347	2.30/0.19	0.00	0.00	0.03	0.07	3.07/0.76	0.10	0.13	0.14	0.38
SIC-S392	2.30/0.19	0.00	0.04	0.06	0.10	3.07/0.76	0.10	0.18	0.29	0.37
SIC-S412	2.30/0.19	0.00	0.03	0.04	0.06	3.07/0.76	0.10	0.15	0.19	0.24
SIC-S643	2.30/0.19	0.02	0.05	0.08	—	3.07/0.76	0.14	0.22	0.25	—
SIC-S762	2.30/0.19	0.00	0.00	0.00	—	3.07/0.76	0.11	0.21	0.24	—
SIC-606	2.30/0.19	0.00	0.07	0.14	—	3.07/0.76	0.10	0.26	0.54	—
SIC-678	2.30/0.19	0.03	0.11	0.23	—	3.07/0.76	0.10	0.38	0.78	—
SIC-679	2.30/0.19	0.05	0.14	0.26	—	3.07/0.76	0.10	0.39	0.77	—
BGRI-824	2.30/0.19	0.00	0.04	0.09	—	3.07/0.76	0.10	0.25	0.42	—
BGRI-826	2.30/0.19	0.01	0.07	0.16	—	3.07/0.76	0.15	0.36	0.65	—
BTCP-2133	2.30/0.19	0.00	0.04	0.05	0.05	3.07/0.76	0.10	0.13	0.20	0.23
BTCP-2162	2.30/0.19	0.01	0.03	0.06	0.06	3.07/0.76	0.10	0.19	0.30	0.30
BTCP-5615	2.30/0.19	0.00	—	—	—	3.07/0.76	0.10	—	—	—
BTCP-5618	2.30/0.19	0.00	—	—	—	3.07/0.76	0.12	—	—	—
BTCP-5658	2.30/0.19	0.00	0.00	—	—	3.07/0.76	0.12	0.27	—	—

^a 15 rad/h.

^b 100 rad/h.

^c 500 rad/h.

^d 1000 rad/h.

Table 7 lists numerical results of fits for 16 samples listed in Table 4. Consistent fit with two common radiation induced color centers at the same energy and with the same width was found for all samples. One broad center is at a wavelength of 400 nm (3.07 eV) with a width of 0.76 eV, and other narrow center is at a longer wavelength of 540 nm (2.30 eV) with a width of 0.19 eV. This observation is similar to that observed in doped BGO samples [23], where three common radiation induced absorption bands were observed for BGO samples doped with different dopants, indicating that the radiation induced color centers are presumably not impurity specific rather lattice structure related. This observation is also consistent with our previous assumption [3,4] that the oxygen vacancies, which are lattice structure defects, are responsible for radiation damage in PbWO₄ crystals.

5. Summary

Yttrium doping is found to shift the emission to blue with a broad spectrum peaked at 420 nm. It is also effective in reducing slow scintillation component, and leading to PbWO₄ crystals with adequate radiation hardness for the CMS experiment. With Y doping it is not necessary to implement oxygen compensation, which is a tedious process. The concentration of Y ions in PbWO₄ crystals is rather uniform. The segregation coefficient of Y in PbWO₄ crystals is determined to be 0.91 ± 0.04 .

The radiation induced absorption in all samples can be decomposed into two color centers with two common centers peaked at wavelengths of 400 nm (3.07 eV) and 540 nm (2.30 eV) with widths of 0.76 and 0.19 eV, respectively. These centers are not as deep as that in Sb doped samples [15]. This explains a relatively large dose rate

dependence of radiation damage and relatively large damage speed in Y doped PbWO₄ crystals.

Acknowledgements

The BTCP samples investigated in this report were provided by Drs. P. Lecoq and P. Lecomte. The BGRI samples were provided by Dr. Mingrong Zhang. Part of the GDMS data used in this report was provided by Dr. P. Lecomte. Many interesting discussions with Drs. H.F. Chen, P. Lecomte, F. Nessi and D.S. Yan are acknowledged. This work is supported in part by U.S. Department of Energy Grant No. DE-FG03-92-ER40701.

References

- [1] Compact Muon Solenoid Technical Proposal, CERN/LHCC 94-38, LHCC/P1, 1994.
- [2] The CMS Electromagnetic Calorimeter Project, CERN/LHCC 97-33, 1997.
- [3] R.Y. Zhu, et al., Nucl. Instr. and Meth. A 376 (1996) 319.
- [4] R.Y. Zhu, et al., IEEE Trans. Nucl. Sci. NS-45 (1998) 686.
- [5] A.N. Annenkov et al., CMS NOTE 1997/055.
- [6] M. Nikl, et al., J. Appl. Phys. Lett. 82 (1997) 5758.
- [7] R.Y. Zhu, IEEE Trans. Nucl. Sci. NS-44 (1997) 468.
- [8] Z.Y. Wei, et al., Nucl. Instr. and Meth. A 297 (1990) 163.
- [9] P. Lecoq, et al., Nucl. Instr. and Meth. A 365 (1995) 291.
- [10] M. Kobayashi, et al., Nucl. Instr. and Meth. A 399 (1997) 261.
- [11] M. Kobayashi, et al., Nucl. Instr. and Meth. A 404 (1998) 109.
- [12] S. Baccaro, et al., Phys. Status Solidi A 164 (1997) R9.
- [13] E. Auffray, et al., Nucl. Instr. and Meth. A 402 (1998) 75.
- [14] Q. Deng, et al., Nucl. Instr. and Meth. A 438 (1999) 415.
- [15] X.D. Qu, et al., Nucl. Instr. and Meth. A 469 (2001) 193.
- [16] Z.W. Yin, et al., in: V. Mikhailin (Ed.), Proceedings of the Fifth International Conference on Inorganic Scintillators and their Applications, Moscow State University, 2000, p. 206.
- [17] M. Kobayashi, et al., Nucl. Instr. and Meth. A 373 (1996) 333.
- [18] R.Y. Zhu, Nucl. Instr. and Meth. A 413 (1998) 297.
- [19] G. Bakhshiva, A. Morozov, Sov. J. Opt. Technol. 44 (1977) 9.
- [20] X.D. Qu, et al., IEEE Trans. Nucl. Sci. NS-47 (2000) 1741.
- [21] J. Rander, in: G. Barreira, et al., (Eds.), Proceedings of the Eighth International Conference on Calorimetry in High Energy Physics, World Scientific, Singapore, 2000, p. 423.
- [22] L.Y. Zhang, et al., CMS Internal Note 1999/014.
- [23] R.Y. Zhu, et al., Nucl. Instr. and Meth. A 302 (1991) 69.